Ultralow-Power Microwave Frequency Comb at a Bistable Phase Transition

Hanfeng Wang,[1,*] Kurt Jacobs,[2,3] Dirk R. Englund,[1] and Matthew E. Trusheim[1,2,†]
[1]Massachusetts Institute of Technology, 50 Vassar Street, Cambridge, Massachusetts 02139, USA
[2]U.S. Army DEVCOM Army Research Laboratory, Adelphi, Maryland 20783, USA
[3]Department of Physics, University of Massachusetts Boston, Boston, Massachusetts 02125, USA

(Received 11 August 2025; accepted 29 January 2026; published 6 April 2026)

Nonlinear phenomena underpin a broad array of technologies, from electronic frequency mixers and harmonic generation to parametric amplification and optical frequency doubling. Conventional schemes for generating microwave frequency combs are constrained by intrinsic material or junction properties that require high driving powers. Here, we overcome these limitations via phase-transition physics. We show that a hybrid quantum system—composed of a solid-state spin ensemble and a nonlinear oscillator—exhibits a distinct bistable phase transition point (BP) where system response becomes both highly enhanced and nonlinear. The nonlinearity around the BP is higher order than other phase transitions, such as exceptional points, critically producing high-order frequency response which enhances nonlinear processes. Approaching the BP, we demonstrate a frequency comb with a record number of teeth at unprecedentedly low driving powers, surpassing previous results using magnonic systems and traditional diode-based approaches. These findings highlight the potential of hybrid quantum systems in advancing high-performance frequency manipulation.

DOI: 10.1103/59xl-zyxp

Subject Areas: Atomic and Molecular Physics, Electronics, Quantum Physics

I. INTRODUCTION

Frequency combs (FCs), coherent electromagnetic spectra with equally spaced frequency components, underpin precision spectroscopy, metrology, and quantum technology because of their exceptional spectral purity, coherence, and stability [1–3]. Comb generation fundamentally exploits nonlinear processes such as saturable absorption, electro-optic modulation, or parametric mixing, which establish a well-defined phase relationship among the equidistant comb teeth [4–7]. In the electrical domain, microwave frequency combs (MFCs) that generate phase-locked, multitone microwave spectra have recently been shown to offer significant advantages over traditional single-frequency or broadband excitation. These benefits span a range of sensing and communication applications, including ultrasensitive micromechanical and passive-radar-like detection [8,9], multifrequency sources for spaceborne microwave instrumentation [10], and dual-comb schemes for underwater ranging [11]. Beyond such established uses, MFCs are also emerging as powerful tools for multitone quantum control and cryogenic microwave electronics [12]. Traditional approaches for harmonic generation in the microwave regime predominantly utilize diode-based devices, leveraging the strongly nonlinear current-voltage (I-V) junction response exhibited when the input voltage surpasses the thermal voltage limit ($V > k_B T/q$) [13–18]. An alternative route involves magnonic FCs [19–24] or phononic FCs [25–29], which exploit intrinsic material nonlinearities such as Kerr or second-order nonlinear interactions inherent to their systems. However, these techniques typically require significant driving power (exceeding 0 dBm) to trigger efficient comb formation, a limitation fundamentally imposed by either the nonlinear junction physics in diode devices or the intrinsic material properties governing magnon or phonon dynamics.

An exciting approach uses coupled linear devices to construct a nonlinear hybrid system, bypassing reliance on intrinsic material nonlinearity and potentially exceeding individual device performance. In particular, coupled non-Hermitian systems can exhibit phase transitions near singularities in the parameter space where system dynamics become nonlinear [30,31]. Exceptional points (EPs) are such singularities, characterized by the coalescence of eigenstates and eigenvalues between coupled systems, and manifest unique phenomena such as unidirectional lasing and topologically protected chiral state transfer [32–40]. The nonlinear effects, which are significantly enhanced near these EPs [30,31,41–47], offer substantial advantages for frequency comb generation at substantially

*Contact author: hanfengw@mit.edu
†Contact author: matthew.e.trusheim.civ@army.mil

Published by the American Physical Society under the terms of the Creative Commons Attribution 4.0 International license. Further distribution of this work must maintain attribution to the author(s) and the published article's title, journal citation, and DOI.

reduced power levels. Recent investigations have successfully employed EP-induced non-Hermitian dynamics for efficient low-power magnonic frequency comb generation, achieving combs with up to 32 spectral teeth [48] with $P \sim 0$ dBm—comparable to conventional electronic-based MFC generation. Nevertheless, these passive EPs systems are known to have several limits: a square-root scaling compared to other higher-order nonlinear responses, external driving source, and limited resolvability of the passive EPs as the operating coupling strength is less than the system linewidth [44,45,47,49–51]. This results in a limited number of comb teeth under low driving power, accompanied by a large harmonic roll-off of 8 dB/harmonic.

In this work, we address and overcome previous limitations by employing an above-threshold, self-oscillating MFC composed of a nitrogen-vacancy (NV) spin ensemble [52–54] coupled to a microwave cavity [55–59]. By integrating a nonlinear Van der Pol (VdP) oscillator through a feedback amplifier, we identify a phase transition point termed the bistable transition point (BP) [60]. Compared to EP systems, BP demonstrates significantly enhanced higher-order nonlinearities, thereby drastically reducing the required power threshold for frequency comb generation. Furthermore, the intrinsic self-sustaining nature of the oscillator eliminates the need for coherent external microwave pump fields in the gigahertz, simplifying the system's operational demands and reducing the power budget. Crucially, the enhanced higher-order response of the BP becomes dominant for high harmonic generation and leads to significantly enhanced comb width. The combination of these effects results in our successful demonstration of microwave frequency combs with an unprecedented number of comb teeth (∼200) at a record-low driving power of −16 dBm. This significant advancement lays a robust foundation for future developments in nonlinear microwave processes, including wireless sensing, communications, and toward quantum hybrid technologies. This technique could also be extended to other above-threshold self-oscillating systems in the electronic domain [61–64] and to the widely used optical frequency combs [5,30,31].

II. NONLINEAR NV MFC SYSTEM

The mechanism underlying frequency mixing and comb generation is illustrated in Fig. 1(a). An optically polarized NV spin ensemble is coupled to a VdP oscillator composed of a microwave resonator and feedback amplifier. As the coupled system operates above its oscillation threshold, it intrinsically generates a coherent self-oscillation at frequency ω_0. The Hamiltonian to describe this system could be written as

$$H_{\text{eff}} = \begin{pmatrix} \omega_c + iG(\alpha)/2 & g \\ g & \omega_s - i\Gamma/2 \end{pmatrix}. \tag{1}$$

Here ω_c is the cavity frequency, ω_s is the spin ensemble center frequency, Γ is the spin linewidth, and g is the effective coupling strength between the two systems. We model the nonlinearity of the feedback gain as $G(\alpha) = G_0 - \kappa/2 - \gamma_s|\alpha|^2$ with G_0 the one-photon gain, κ is the cavity linewidth, α is the cavity field, and γ_s denotes the nonlinear damping rate due to amplifier saturation.

Solving the coupled-mode equations yields a cubic relation for the steady-state oscillation frequency. When $\Delta_g = \Gamma/2 - g < 0$, the system enters a bistable region arising from the nonlinear response. This bistability collapses nonadiabatically once the spins are detuned from the cavity resonance, as illustrated in Fig. 1(b). As the coupling strength decreases, the detuning window that supports bistability narrows and eventually vanishes. Beyond this point ($\Delta_g > 0$), only a single real solution for the oscillation frequency exists, and the critical point where bistability disappears is identified as the BP ($\Delta_g = 0$). Importantly, the NV VdP system always maintains a stable steady state above the gain threshold—even near the BP or under detuning—contrasting with a conventional EP, where small perturbations often drive the solutions into unstable, lossy, or diverging behavior.

Around the BP, the response of the system is strongly modified. We plot the linecut of the Riemann surface along $\Delta_g = 0.6$ kHz in Fig. 1(c). The oscillating frequency around the resonance condition ($\Delta_s = 0$) could be expressed as (see Appendix A 1)

$$\Delta = \sum_{k=0}^{\infty} \xi^{(2k+1)} \Delta_s^{2k+1}. \tag{2}$$

Note that the Taylor expansion includes only odd-order terms due to the symmetry. Here we have parametrized the response to identify the contributions at different orders in input field: $\xi^{(1)} \propto 1/\Delta_g$ is the linear response (effective gyromagnetic ratio), $\xi^{(3)} \propto 1/\Delta_g^4$ is the third-order nonlinear coefficient, and further terms are contained within the summation (see Appendix A 1 for the explicit expressions). The oscillation frequency of the system can be modulated through variations in the spin frequency ω_s (or equivalently, the detuning Δ_s), which in practice is induced by an external magnetic field via the Zeeman effect, i.e., $\Delta_s = \gamma_e B \cos(\omega_d t)$, where γ_e is the bare-electron spin gyromagnetic ratio. In the sensing application [56], approaching the BP ($\Delta_g \to 0$) enhances $\xi^{(1)}$, resulting in an inverse-linear amplification of the VdP oscillator's frequency response [Fig. 1(c), red line] over pure electron response. This scaling significantly surpasses that of the EP system (see Appendix A 3). We further demonstrated that this amplification does not introduce compensated noise, thereby improving the overall SNR [60].

The nonlinear contributions associated with frequency mixing, such as $\xi^{(3)}$, $\xi^{(5)}$, and higher-order terms, also

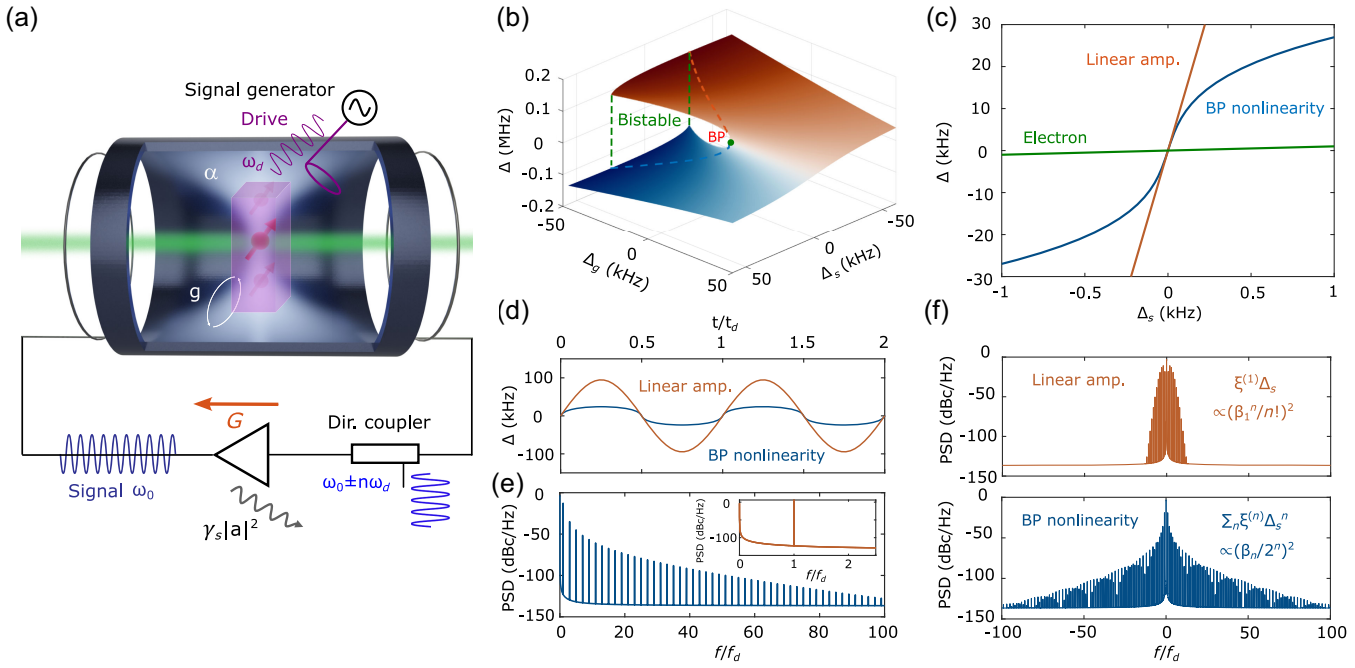


FIG. 1. NV-MFC concept. (a) Schematic illustrating the hybrid system containing an optically polarized NV ensemble and a VdP oscillator. The VdP oscillator is characterized by a cavity mode a with loop gain G and an amplifier nonlinear saturation parameter γ_s. The spin ensemble features a linewidth Γ and couples effectively to the cavity mode with strength g. A bias field at frequency ω_d, generated by a separate signal generator, drives frequency comb formation. The output signal, extracted through a directional coupler, contains harmonics with frequencies $\omega_0 \pm n\omega_d$. (b) Simulated surface plot depicting the oscillation frequency as a function of gain detuning Δ_g and spin detuning Δ_s. The dashed lines indicate a bistable region where two stable solutions coexist, merging at BP. (c) Blue: 1D linecut of the simulated oscillating frequency along $\Delta_g = 0.6$ kHz. Red: first-order (linear) approximation of the BP response. Green: bare-electron response without BP enhancement. (d) Simulated time domain dynamics of the oscillation frequency with BP nonlinearity (blue) and linear amplification (red). The time is normalized by the driving field period $t_d = 1/f_d$, with f_d the frequency of the driving field. (e) Simulated power spectral density of nonlinear phase response (blue) and linear amplification (red). (f) Example simulated frequency comb generated by the full NV MFC system with BP nonlinearity (blue) and an considering only the enhanced linear response (red). PSD: Power spectral density.

increase sharply near the BP. A comparison between a pure linear response and the BP instantaneous oscillation frequency is plotted in Fig. 1(d). The linear amplification case yields an almost perfect sinusoidal response, while the presence of BP-induced nonlinearity distorts the waveform into a triangular shape with Fourier components shown in Fig. 1(e).

The output voltage $v(t)$ from the cavity-coupled NV system associated with this frequency modulation can be expressed as

$$v(t) = V_0 \cos\left[\omega_0 t + \int_0^t \sqrt{2}\frac{d\Delta}{d\Delta_s}\Delta_s d\tau\right]. \quad (3)$$

Here V_0 is the voltage corresponding to the cavity oscillating power. We first consider the linear contribution of the Taylor expansion in Eq. (3) with the BP-enhanced small-signal amplification. Because of the sinusoidal varying phase, sidebands with frequency $\omega_0 \pm n\omega_d$ emerge with power given by $P_n \propto J_n(\beta_1)^2 = [(\beta_1/2)^n/n!]^2$, where $\beta_1 = \sqrt{2}\xi^{(1)}\gamma_e B/\omega_d$ and J_n is the nth-order Bessel function of the first kind. As a result, the sideband power of the nth comb tooth scales factorially, as illustrated in Fig. 1(f), top.

By contrast, when higher-order nonlinear terms are included, the power can be expressed as $P_n \propto J_1(\beta_n)^2 = (\beta_n/2)^2/2^{2n-2}$, with $\beta_n = \sqrt{2}\xi^{(n)}(\gamma_e B)^n/\omega_d$ $(n = 2k+1)$. This relation follows an exponential scaling with n, as shown in Fig. 1(f) bottom, which leads to a pronounced enhancement of high-order comb teeth above the phase noise floor. In addition to generating a larger number of comb teeth, we also observe that the odd and even orders of the MFC exhibit significantly different powers. This asymmetry arises because the nonlinear terms are odd with respect to the drive field, resulting in enhanced comb power for the $n = 2k+1$ components.

The BP system then combines two strong effects, each dominant in different regimes. The dramatic enhancement of linear response enables the condition $\gamma B/\omega_d \gg 1$ at low magnetic field strengths (input drive powers). Under these conditions, the output spectrum comprises numerous harmonics at frequencies $\omega_s \pm n\omega_d$ as an overdriven frequency modulation scheme [65,66]. Second, the high-order

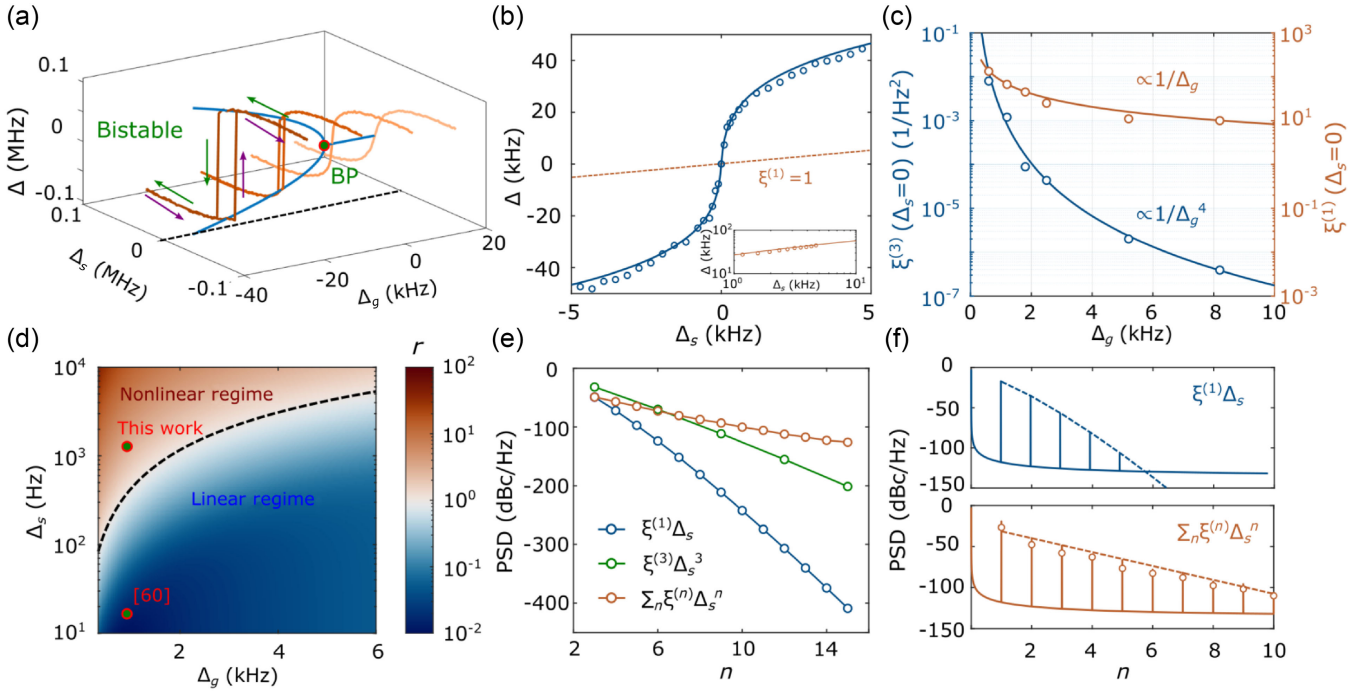


FIG. 2. BP nonlinearity. (a) Self-oscillating spectrum. A bistable regime and a single-valued regime is separated by the BP. Which regime the system is in depends on the detuning in coupling strength Δ_g (tuned by the oscillating power via spin-saturation effects) and spin-cavity detuning Δ_s (tuned by a static external magnetic field). The blue line shows the oscillation frequency Δ when $\Delta_s = 0$. (b) Oscillation frequency Δ as a function of detuning Δ_s at $\Delta_g = 0.6$ kHz. Inset: logarithmic plot of system response indicating cube-root scaling. Line: simulation results. Dots: experimental data. (c) Third-order nonlinear coefficient $\xi^{(3)}$ (blue) and linear coefficient $\xi^{(1)}$ (red) as a function of Δ_g. They follow the different scaling with $\xi^{(3)} \propto 1/\Delta_g^4$ and $\xi^{(1)} \propto 1/\Delta_g$. Line: simulation results. Dots: experimental data. (d) The ratio between the third-order nonlinear and linear contributions to frequency modulation ($r = \xi^{(3)}\Delta_s^3/\xi^{(1)}\Delta_s$) as a function of Δ_s and Δ_g. The linear and nonlinear regimes are separated by $r = 1$. We marked our previous sensing work [60] as the green dot. (e) Simulated nth MFC power induced by the linear ($\xi^{(1)}\Delta_s$, red), the third-order nonlinear ($\xi^{(3)}\Delta_s^3$, green), the full nonlinear terms ($\sum_n \xi^{(n)}\Delta_s^n$) components given $\Delta_s = 100$ Hz. (f) Top: the MFC teeth driven by the linear term $\xi^{(1)}\Delta_s$. Dashed line: factorial fit $[(\beta_1/2)^n/n!]^2$. Bottom: the MFC teeth driven by the combination of linear and nonlinear terms $\sum_n \xi^{(n)}\Delta_s^n$. Dots. experimental data; dashed line, exponential-decay fit.

components of the BP nonlinearity offer a way to bypass the Γ-function factorial decay in Bessel functions at high orders. These two effects, engineered in an otherwise linearly coupled system, result in ultralow-power, wide-band MFCs.

III. EXPERIMENTAL DEMONSTRATION OF BP-ENHANCED NONLINEARITY

We first experimentally demonstrate the self-oscillation and BP behavior in our system. Figure 2(a) presents the oscillation frequency spectrum as a function of spin detuning Δ_s and gain detuning Δ_g. A clear transition emerges between two distinct operational regimes—bistable and single-valued—delineated precisely by the BP. Experimentally, Δ_g is tuned by varying the input microwave power. As reported in our previous work [55], increasing the microwave power drives spin Rabi transitions and depolarizes the spin ensemble, thereby effectively reducing the coupling strength g and broadening the spin linewidth (see Appendix A 6).

We next demonstrate the predicted frequency response near the BP. Figure 2(b) shows the self-oscillation frequency as a function of spin detuning Δ_s, tuned via a variable bias magnetic field at a fixed coupling offset $\Delta_g = 0.6$ kHz. In the small-signal regime ($\Delta_s < 250$ Hz), we observe a linear response with an amplification factor of $\xi^{(1)} = 135$, which transitions smoothly to a nonlinear cubic-root scaling ($\Delta \propto \Delta_s^{1/3}$) once the spin detuning exceeds the coupling offset ($\Delta_s > \Delta_g$). These experimental observations are in excellent agreement with predictions from the quantum Heisenberg model (see Appendix A 3).

To further investigate the nonlinear behavior near the BP, we extract the third-order nonlinear coefficient $\xi^{(3)}$ as a function of the detuning Δ_g, as shown in Fig. 2(c). The data follow the theoretically predicted fourth-order scaling, $\xi^{(3)} \propto 1/\Delta_g^4$, indicating that $\xi^{(3)}$ grows much more rapidly

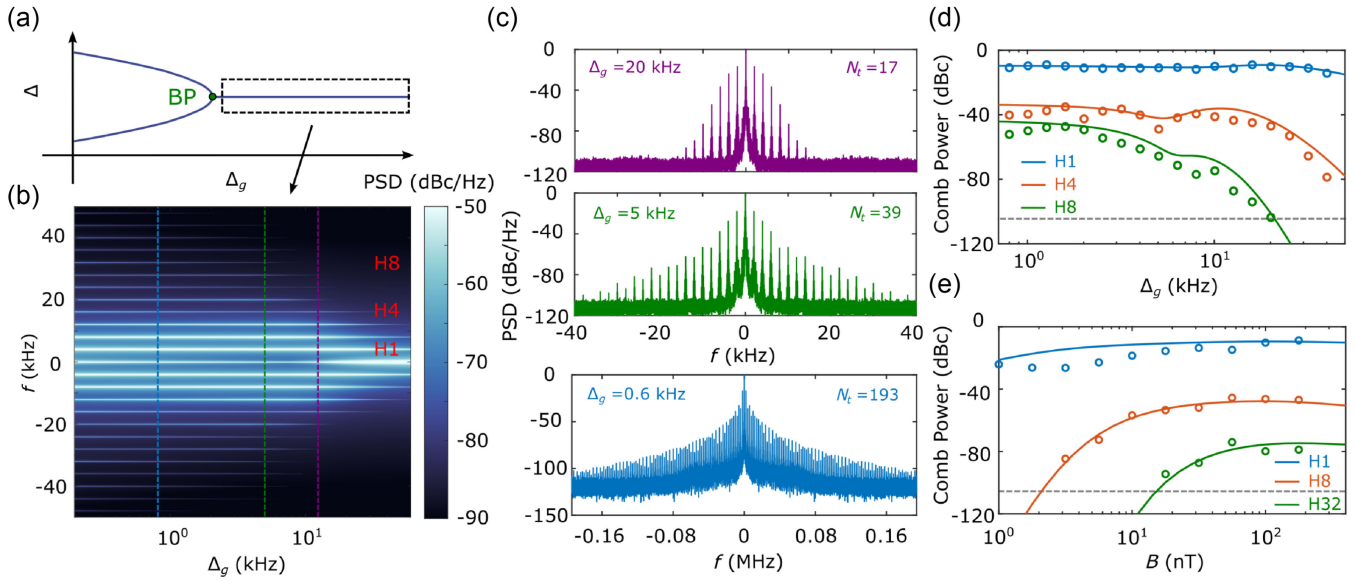


FIG. 3. BP-enhanced NV MFC. (a) Schematic of BP response. We operate the NV MFC in the single-valued regime ($\Delta_g > 0$). (b) Power spectra of the mode as a function of Δ_g with a driving field with amplitude $B = 177$ nT and comb spacing frequency $\omega_d = 2$ kHz. Clearly resolved, equally spaced spectral peaks are separated by ω_d. Additional satellites appear when approaching the BP due to the enhanced nonlinearity and effective gyromagnetic ratio. (c) Frequency combs generated by the NV MFC system at gain detunings $\Delta_g = 20$ kHz (purple, 17 satellites), $\Delta_g = 5$ kHz (green, 39 satellites), and $\Delta_g = 0.6$ kHz (blue, 193 satellites). (d) Amplitude of the harmonics H1 (blue), H4 (red), and H8 (green) as a function of Δ_g. Line, NV MFC modeling; dots, experimental data. Dotted line: Phase noise. (e) Amplitude of the harmonics H1, H8, and H32 as a function of driving magnetic field. Line: NV MFC modeling; dots, experimental data.

than the linear term $\xi^{(1)} \propto 1/\Delta_g$. To quantify the deviation from linearity, we define a normalized ratio $r = (\xi^{(1)}\Delta_s - \Delta)/\Delta$, which measures the deviation between the observed oscillation frequency Δ and the expected linear response $\xi^{(1)}\Delta_s$, as shown in Fig. 2(d). In our previous work, the system operated in the linear regime ($r \ll 1$, red circle), whereas here we access the strongly nonlinear regime ($r \gg 1$). Notably, for $\Delta_s > 300$ Hz and $\Delta_g = 0.6$ kHz, the nonlinear response exceeds the linear contribution ($r > 1$). This crossover corresponds to a driving magnetic field of approximately 20 nT, or equivalently a microwave power of −44 dBm, required to initiate nonlinear behavior—substantially lower than that reported in prior demonstrations of magnonic-, phononic-, and electronic-based MFCs [7,27,48].

We then analyze how these nonlinearities contribute to the generation of MFCs. Figure 2(e) shows the comb power at different orders, driven respectively by the linear response term ($\xi^{(1)}\Delta_s$) and the third-order nonlinear component ($\xi^{(3)}\Delta_s^3$) for $\Delta_s = 100$ Hz. Since $\Delta_s \ll \Delta_g$, the Taylor expansion of Eq. (2) remains valid, allowing higher-order terms to be treated perturbatively. The frequency comb generated by the linear response exhibits a factorial decay of power, $P_1 \propto (1/n!)^2$, whereas that arising from the third-order nonlinearity scales as $P_3 \propto [1/(n/3)!]^2$. When contributions from all nonlinear orders are included, the overall comb envelope follows an exponential decay, consistent with the experimentally observed spectral profile shown in Fig. 2(f). We fit the measured power spectra of individual comb teeth with factorial (blue) and exponential (red) decay functions to highlight the transition from linear to nonlinear scaling behavior.

Throughout this analysis, we restricted our discussion to the regime where the driving field satisfies $\Delta_s \ll \Delta_g$, ensuring that the Taylor expansion in Eq. (3) around $\Delta_s = 0$ remains valid (see Appendix A 1). In Sec. IV, we further present the experimental and numerical results for the regime $\Delta_s \gg \Delta_g = 0.6$ kHz, where the system enters the strongly driven domain.

IV. STRONGLY DRIVEN NV MFC

We now characterize the NV MFC system, leveraging the enhancement provided by the BP in the strongly driven regime. A drive magnetic field with amplitude $B = 177$ nT is applied at a modulation frequency $\omega_d = 2$ kHz, yielding a spin-detuning amplitude of $\Delta_s = \gamma_e B \approx 4.9$ kHz (see Appendix A 4 for details). This operation lies beyond the validity of the Taylor expansion regime discussed earlier; therefore, we perform numerical simulations to capture the system dynamics in this regime. By systematically investigating the system response as it approaches the BP, as indicated in Fig. 3(a), we reveal how the enhanced nonlinearity reshapes the frequency

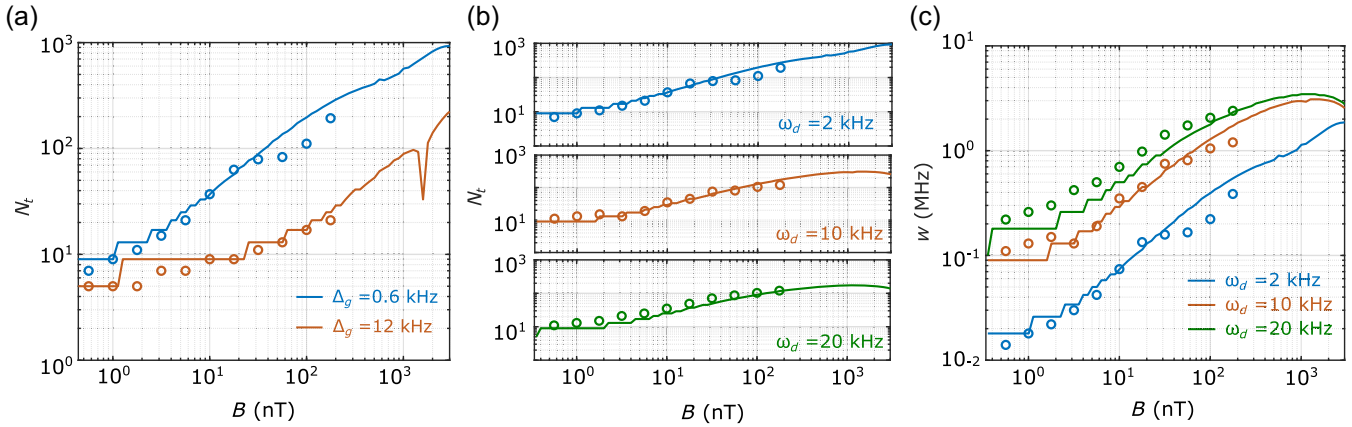


FIG. 4. NV MFC performance. (a) Number of teeth N_t as a function of seed field strength B when $\Delta_g = 12$ kHz (red) and $\Delta_g = 0.6$ kHz (blue). Line, NV MFC modeling; dots, experimental data. (b) Number of teeth as a function of bias magnetic field B for different tooth spacing $\omega_d = 2$ kHz, 10 kHz, and 20 kHz when the system is enhanced by BP ($\Delta_g = 0.6$ kHz). Line, NV MFC modeling; dots, experimental data. The number of teeth is almost independent with the driving magnetic field B. (c) MFC bandwidth as a function of driving power for different tooth spacing $\omega_d = 2$ kHz, 10 kHz, and 20 kHz. Line, NV MFC modeling; dots, experimental data.

comb generation process and modifies the resulting spectral characteristics.

Figure 3(b) presents power spectra illustrating frequency comb generation at varying values of gain detuning Δ_g. We observe clearly resolved, evenly spaced spectral peaks separated by the modulation frequency ω_d. When operating far from the BP, only a limited number of comb lines are observed. As the system approaches the BP, additional satellite peaks appear, significantly enhancing the comb density. This behavior is experimentally demonstrated in Fig. 3(c), where the comb expands from 17 satellites at $\Delta_g = 20$ kHz to 193 satellites at $\Delta_g = 0.6$ kHz.

To highlight power dependence for the harmonics on proximity to the BP, we analyze selected harmonics, specifically the first, fourth, and eighth harmonics (H1, H4, H8), as shown in Fig. 3(d). We observe minimal change in the power of H1 as the BP is approached due to the saturation of the corresponding Bessel function $J_1(\beta)$, where $\beta = \gamma B/\omega_d \sim 1$ (see Appendix A 3). Conversely, higher-order harmonics initially have rapidly diminishing amplitudes under similar conditions. However, approaching the BP dramatically enhances the effective gyromagnetic ratio and nonlinear curvature, elevating these harmonics significantly above the phase noise floor. Ultimately, harmonic amplitudes saturate near the BP as they enter the oscillatory regime, becoming insensitive to variations in β (see Appendix A 3). We then fix the $\Delta_g = 0.6$ kHz and vary the driving field amplitude B. With the driving field of 177 nT, corresponding to a driving power of −16.6 dBm. The H32 component remains 30 dB above the phase-noise floor, yielding a total of 193 comb teeth, as shown in Fig. 3(c) (bottom) and Fig. 3(d). This is one order larger than the EP-enhanced magnonic frequency comb [48] given a power level decrease for 2 orders of magnitude.

We then plot the number of teeth, which is seen as a critical figure of merit in MFC systems [19,48], in Fig. 4(a). Near the BP, specifically at $\Delta_g = 0.6$ kHz, the number of teeth initially grows with driving field B, following a square-root scaling law. However, it saturates at $B = 0.8\,\mu$T with a theoretically largest possible $N_t \sim 400$ given a driving power of 4 dBm. This number surpasses the state-of-the-art number of comb teeth by an order of magnitude [48].

Finally, we demonstrate that the BP-enhanced MFC allows tunable teeth spacing ω_d while maintaining a stable number of teeth. As illustrated in Fig. 4(b), the comb retains a consistent tooth count at fixed coupling offset and power as the spacing frequency varies from 2 to 20 kHz within the low driving regime. However, increasing the tooth spacing beyond this regime significantly reduces the maximum achievable number of teeth. This reduction occurs because the intrinsic frequency modulation amplitude inversely scales with the offset frequency. In the low driving power regime, the system operates in a regime characterized by $\gamma/\gamma_e \gg 1$, resulting in $\beta = \gamma B/\omega_d \gg 1$. Under these conditions, the Bessel functions $J_k(\beta)$ enter an oscillatory regime, effectively removing dependence on the offset frequency ω_d. Conversely, at higher driving powers, reductions in both effective gyromagnetic ratio and higher-order nonlinearity lead to fewer comb teeth at larger tooth spacing frequencies. Nevertheless, increasing tooth spacing notably expands the MFC bandwidth, as shown in Fig. 4(c). Ultimately, the achievable tooth spacing and comb bandwidth are constrained by the spin linewidth; when the modulation frequency exceeds the spin linewidth, the spin mode coherence cannot fully reach steady state before

subsequent frequency detunings. Consequently, the system's response diminishes by a factor of $\Gamma/(\Gamma+\omega_d)$.

V. OUTLOOK AND DISCUSSION

We compare the performance of the BP-enhanced NV MFC with other established harmonic generation techniques in Fig. 5. Two critical figures of merit are the required input microwave power and the harmonic roll-off R, defined as the power drop per harmonic [13–18]. Conventional diode-based harmonic generators, including Schottky, varactor, and step recovery diodes, typically require driving powers in the range of 0 to 20 dBm, with harmonic roll-offs between 4 and 12 dB/harmonic [13–18]. Typical magnonic FCs require a high power of microwave drive 20 dBm [23] while phononic or mechanical FCs requires microwave drive around 0 dBm with large R. While recently demonstrated EP-enhanced magnon FC systems have reduced the driving power to 3.8 dBm with an increased harmonic roll-off ($R = 8$ dB/harmonic), the driving power is still comparable with the traditional MFCs [48]. In addition, magnonic FCs require a bias coil to generate ~1 T bias magnetic field with electromagnets. In contrast, our BP-enhanced NV MFC system significantly improves upon these benchmarks, operating effectively at input powers ranging from −36 to −16 dBm ($B = 17.7$ to $B = 177$ nT) while maintaining a competitive harmonic roll-off between 5 and 17 dB/harmonic.

Here we have demonstrated a novel frequency comb generation method leveraging a BP in the NV MFC system. Unlike traditional frequency comb systems that depend heavily on intrinsic material nonlinearities and require substantial power input, our approach achieves significantly enhanced nonlinearities near the BP, thereby dramatically reducing the power threshold necessary for comb generation. By harnessing the self-oscillatory behavior inherent in the VdP oscillator, we eliminate the need for external high-frequency microwave drives, significantly simplifying the operational requirements. Experimentally, our system demonstrates unprecedented performance, including the generation of microwave frequency combs with approximately 200 satellites at orders-of-magnitude lower drive power.

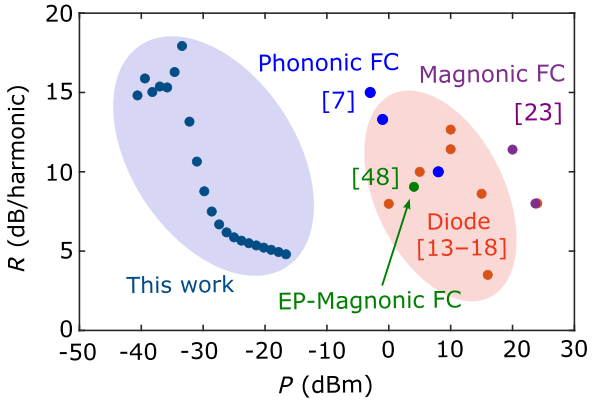


FIG. 5. MFC benchmark. The harmonic roll-off R and driving power P for different operating systems. Red: diode-based wideband harmonic generation [13–18]. Dark blue: NV MFC under different driving powers. Green: EP-enhanced magnonic FC [48]. Purple: magnonic FC [23]. Light blue: Phononic FC [7]. The NV VdP system maintains the small harmonic roll-off R while operating in a relatively low microwave power.

Future research could focus on optimizing the NV MFC system's robustness and stability, particularly with respect to long-term phase coherence and comb tooth uniformity. The overall wall-plug power consumption (including laser pumping) and size of the system are areas with significant potential for improvement (see Appendix A 10). Polarization of $N = 10^{14}$ spins with relaxation time $T_1 \sim 6$ ms requires $N_{\mathrm{ph}} \sim 10^{17}$ photons/ sec, which corresponds to roughly 10 mW optical power to bias the system to the BP. Further optimization to increase the single spin coupling strength (by decreasing the mode volume) or increase T_1 (e.g., by decreasing temperature) will improve the optical power budget. Furthermore, investigating other quantum systems that exhibit similar nonlinear transition points may offer additional pathways for frequency comb generation with even lower power requirements and higher performance metrics [59,67,68]. Exploring the integration of such hybrid quantum systems onto chip-scale platforms could significantly impact scalable quantum technologies, including quantum computing architectures and ultrasensitive quantum sensors, ultimately paving the way for high-performance devices across a wide range of real-world applications.

More broadly, the present work highlights NV-based hybrid systems as a promising platform for exploring nonlinear behaviors beyond typical sensing and networking applications. The coexistence of multiple, distinct nonlinear mechanisms (BP nonlinearity, spin saturation-induced nonlinearity [69]) in coupled NV-cavity systems, together with the potential to tune between semiclassical collective dynamics and quantum spin coherence [70,71], opens new opportunities to study EP-like physics and nonlinear phenomena in regimes that are not readily accessible in conventional classical or purely bosonic platforms.

ACKNOWLEDGMENTS

H. W. acknowledges support from Bosch Inc. D. R. E. acknowledges funding from the MITRE Corporation.

H. W. and K. J. developed the theory. H. W. conducted the experiments. H. W and M. E. T. conceived of the device concept. H. W. and M. E. T. prepared the manuscript. All authors discussed the results and revised the manuscript. M. E. T. and D. R. E. supervised the project.

The authors declare that they have no competing interests.

DATA AVAILABILITY

The data that support the findings of this article are openly available [72].

APPENDIX

1. NV MFC model

We start from the linear coupled NV-cavity hybrid system described in previous works [55]. Then we route the output field from the cavity through an amplifier and subsequently feed it back into the cavity, as shown in Fig. 1(a). This feedback introduces an additional term, $G\alpha$, into the equation of motion for cavity field α. However, as the input power to the amplifier, given by $\kappa|\alpha|^2$ (corresponding to the input field amplitude $\sqrt{\kappa}\alpha$), increases, the amplifier's gain correspondingly decreases. To capture this behavior, we consider a specific operating point on the amplifier's output characteristic and perform a first-order expansion around that point. This allows us to express the gain reduction as a linear function of $|\alpha|^2$. The coupled mode equations with cavity field α and spin coherence s become

$$\begin{aligned}\dot{\alpha} &= -(\kappa/2 - [G - \gamma_s|\alpha|^2])\alpha - igs,\\ \dot{s} &= -[\Gamma/2 + i\Delta_s]s - ig\alpha.\end{aligned} \tag{A1}$$

Substituting the ansatz $\alpha(t) = \alpha e^{i\Delta t}$ and $s(t) = se^{i\Delta t}$, the steady-state solution for Δ could be expressed as

$$\begin{aligned}-i\Delta\cdot\alpha &= (G - \kappa/2 - \gamma_s|\alpha|^2)\alpha - igs.\\ -i\Delta\cdot s &= -(\Gamma/2 + i\Delta_s)\alpha - ig\alpha.\end{aligned} \tag{A2}$$

By separating these equations into their real and imaginary parts, we can write the solution as

$$\begin{aligned}G - \frac{\kappa}{2} - \gamma_s|\alpha|^2 &= \frac{\Gamma}{2},\\ s &= \frac{-ig}{\Gamma/2 + i\Delta_s - i\Delta}\alpha.\end{aligned} \tag{A3}$$

This means that when the system is on resonance, the gain induced by the amplifier itself perfectly balances the loss by the spin, and it is independent with the amplifier choice. The solution for this coupled-mode equation could be expressed by a cubic equation of Δ:

$$\Delta^3 - 2\Delta_s\Delta^2 + (\Delta_s^2 + \Gamma^2/4 - g^2)\Delta + \Delta_s g^2 = 0, \tag{A4}$$

with prefactors

$$\begin{aligned}c_2 &= -2\Delta_s,\\ c_1 &= \Delta_s^2 + (\Gamma/2)^2 - g^2,\\ c_0 &= \Delta_s g^2.\end{aligned} \tag{A5}$$

The solution for the oscillation frequency Δ could then be expressed as

$$\begin{aligned}\Delta = &\frac{1}{3\sqrt[3]{2}}\sqrt[3]{-2\Delta_s^3 - 9\Delta_s[g^2 + 2(\Gamma/2)^2] - 3\sqrt{3}\sqrt{4\Delta_s^2(\Gamma/2)^2 - 4[g^2 - (\Gamma/2)^2]^3} + \Delta_s^2[-g^4 + 20g^2(\Gamma/2)^2 + 8(\Gamma/2)^4]}\\ &+ \frac{1}{3\sqrt[3]{2}}\sqrt[3]{-2\Delta_s^3 - 9\Delta_s[g^2 + 2(\Gamma/2)^2] + 3\sqrt{3}\sqrt{4\Delta_s^2(\Gamma/2)^2 - 4[g^2 - (\Gamma/2)^2]^3} + \Delta_s^2[-g^4 + 20g^2(\Gamma/2)^2 + 8(\Gamma/2)^4]}\\ &+ \frac{2}{3}\Delta_s.\end{aligned} \tag{A6}$$

This is the expression for plotting the BP nonlinear dependence in Fig. 1. The Taylor expansion of Eq. (A6) around $\Delta_s = 0$ shows

$$\begin{aligned}\Delta &= \left(\frac{g^2 + 2(\Gamma/2)^2}{3(g + \Gamma/2)\Delta_g} + \frac{2}{3}\right)\Delta_s + \frac{g^2(\Gamma/2)^4}{(g + \Gamma/2)^4\Delta_g^4}\Delta_s^3\\ &\quad + \frac{2g^4(\Gamma/2)^6 + g^2(\Gamma/2)^8}{(g + \Gamma/2)^7\Delta_g^7}\Delta_s^5 + \cdots\\ &\equiv \xi^{(1)}\Delta_s + \xi^{(3)}\Delta_s^3 + \xi^{(5)}\Delta_s^5 + \cdots.\end{aligned} \tag{A7}$$

It is worthwhile to note that if we assume $\Delta_g \equiv \Gamma/2 - g = 0$ (BP condition) in Eq. (A21), we have

$$\Delta = -\Delta_s^{1/3}g^{2/3} + \frac{2}{3}\Delta_s, \tag{A8}$$

meaning that the BP is third order (when Δ_s is sufficiently small the slope of the first term dominates).

2. Frequency modulation of the NV MFC system

The frequency modulation system consists of an NV ensemble and a VdP oscillator. The time derivative of the instantaneous phase $\phi(t)$ obeys

$$\frac{d\phi(t)}{dt} = \omega_0 + \gamma_{\text{eff}}B(t). \tag{A9}$$

Here γ_{eff} is the effective gyromagnetic ratio defined as $\gamma_{\text{eff}} \equiv \gamma_e d\Delta/d\Delta_s$, with γ_e the bare-electron gyromagnetic ratio. The oscillator phase could then be expressed as

$$\phi(t) = \int_0^t \sqrt{2}\frac{d\Delta}{d\Delta_s}\Delta_s d\tau. \tag{A10}$$

Constitute Eq. (A7) for the oscillation frequency Δ, we obtain the oscillator phase as

$$\phi(t) = \sum_k \int_0^t \sqrt{2}(2k+1)\Delta_s^{2k+1} d\tau. \tag{A11}$$

We assume the system has a frequency modulation of $\Delta_s(t) = \gamma_e B\cos(\omega_d t)$. Then the above equation becomes

$$\phi(t) = \sum_k \int_0^t \sqrt{2}(2k+1)\xi^{(2k+1)}(\gamma_e B)^{2k+1}\cos^{2k+1}(\omega_d\tau)d\tau. \tag{A12}$$

The integral will consist of many components with different frequencies. To simplify Eq. (A12), we took the highest order in each component of $\cos[(2k+1)\omega_d t]$. The system can then be simplified to

$$\phi(t) = \sum_k \frac{\sqrt{2}}{2^{2k}\omega_d}\xi^{(2k+1)}(\gamma_e B)^{2k+1}\sin[(2k+1)\omega_d t]. \tag{A13}$$

For the linear case described in Ref. [60], the system operates in the linear regime, where $\xi^{(2k+1)}(\gamma_e B)^{2k+1} \ll \xi^{(1)}(\gamma_e B)$; therefore, the phase could then be expressed as

$$\phi(t) = \frac{\sqrt{2}\xi^{(1)}\gamma_e B}{\omega_d}\sin(\omega_d t). \tag{A14}$$

The output spectrum could then be determined using the Jacobi-Anger expansion and the Bessel function identity:

$$\begin{aligned} v &= V_0\cos[\omega_0 t + \phi(t)] = V_0\sum_n J_n(\beta_1)\cos(\omega_0 + n\omega_d)t \\ &= V_0\sum_n \left(\frac{\beta_1}{2}\right)^n \frac{1}{n!}\cos(\omega_0 + n\omega_d)t. \end{aligned} \tag{A15}$$

Here the $J_n(\beta_1)$ is the Bessel function and $\beta_1 \equiv \sqrt{2}\xi^{(1)}\gamma_e B/\omega_d$; see Fig. 6. This shows that the nth comb teeth ($n = 2k+1$) exhibits a power of $(1/n!)^2$.

The nonlinear response, however, offers different scaling compared to the overdriving case of the linear scaling. To simplify the calculation, here we calculate only the strongest contributing component of the nonlinear response to the comb lines, i.e., only the first-order Bessel function

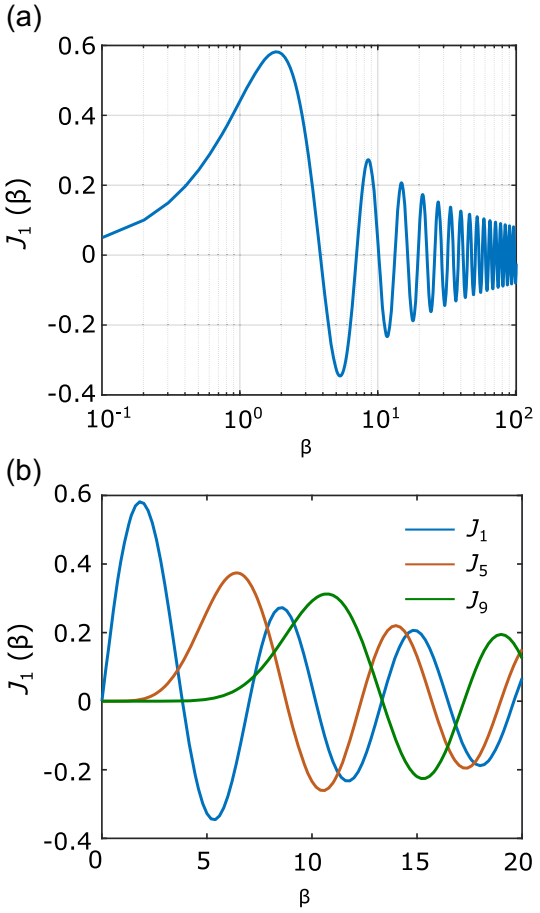


FIG. 6. Bessel functions for frequency modulation. (a) Bessel function $J_1(\beta)$ plotted as a function of β. Two distinct regimes are evident. In the regime where $\beta \ll 1$, the Bessel function is approximately linear, following $J_1(\beta) \propto \beta$. Conversely, for $\beta \gg 1$, the function transitions into a rapidly oscillating regime as β increases. (b) Comparison of higher-order Bessel functions J_1 (blue curve), J_5 (red curve), and J_9 (green curve). As the order of the Bessel function increases, the threshold for entering the oscillation regime shifts linearly to higher β values.

for each nonlinear component and only the odd orders. The phase could then be simplified to

$$\begin{aligned} v &= V_0\cos[\omega_0 t + \phi(t)] \\ &= V_0\sum_k \frac{J_1(\beta_k)}{2^{2k}}\cos[\omega_0 + (2k+1)\omega_d]t \\ &= V_0\sum_k \frac{\beta_k}{2^{2k+1}}\cos[\omega_0 + (2k+1)\omega_d]t, \end{aligned} \tag{A16}$$

with $\beta_k \equiv \sqrt{2}\xi^{(2k+1)}(\gamma_e B)^{2k+1}/\omega_d$. Therefore the comb teeth obeys the exponential decay rather than factorial scaling in the linear regime, given that β_n is comparable to β_1, or the nonlinear terms $\xi^{(2k+1)}$ is comparable to the linear prefactor $\xi^{(1)}$. Therefore, the nth comb teeth has a comb

power $P \propto J_1(\beta_n)^2 = (\sqrt{2}\xi^{(n)}\gamma_e B/\omega_d)^2/2^{2n-2}$, exhibiting a different power scaling of $\propto (1/2^{2n})$. We note that this analysis is constrained in the small-signal regime, where the Taylor expansion and Eqs. (17) and (18) hold. In the large-signal regime shown in Fig. 3, we note that the conclusion holds that the nonlinear regime exhibits a different scaling. We add a constant in the power-to-field conversion relation when fitting the power data in Fig. 3 which may due to the fluctuation of the field in the experiment, though it does not affect the conclusion of the number of teeth, which is the main figure of merit in the article (see Appendix A 8 for more details).

3. Comparison between the BP and EP scaling

We presented the oscillation frequency Δ dependence with detuning Δ_s [Eq. (A8)] for the BP. Here we discuss the scaling of an above-threshold linear EP system for comparison. The EP Hamiltonian can be written as

$$H_{\text{eff}} = \begin{pmatrix} i\Gamma/2 & g \\ g & \Delta_s - i\Gamma/2 \end{pmatrix}. \tag{A17}$$

The eigenvalue for this matrix can be expressed as

$$\Delta_{1,2} = \frac{\Delta_s \pm \sqrt{\Delta_s^2 - 2i\Gamma\Delta_s - 4(\Gamma^2/4 - g^2)}}{2}. \tag{A18}$$

Assuming the detuning Δ_s is much smaller than the spin linewidth $\Gamma/2$ ($\Delta_s \ll \Gamma$), we can ignore the Δ_s^2 term in the above equation. A similar result can also be obtained with Newton-Puiseux series expansion. The relation between Δ and Δ_s can then be expressed as

$$\begin{aligned}\Delta &= \frac{\Delta_s \pm \sqrt{-2i\Gamma\Delta_s - 4(\Gamma^2/4 - g^2)}}{2} \\ &= \frac{\Delta_s \pm \sqrt{-2i\Gamma\Delta_s - 4(\Gamma/2 - g)(\Gamma/2 + g)}}{2}.\end{aligned} \tag{A19}$$

When the system is very close to the EP, namely $\Delta_g = \Gamma/2 - g \sim 0$. We rewrite the last equation Eq. (A19):

$$\begin{aligned}\Delta &= \frac{\Delta_s \pm \sqrt{-2i\Gamma\Delta_s - 4(\Gamma/2 + g)(\Gamma/2 - g)}}{2} \\ &= \frac{\Delta_s}{2} \pm i\sqrt{\frac{\Gamma}{2}}\sqrt{i\Delta_s - 2\Delta_g} \\ &= \frac{\Delta_s}{2} \pm i\sqrt{\frac{\Gamma}{2}}\sqrt[4]{\Delta_s^2 + 4\Delta_g^2 e^{i\phi}}.\end{aligned} \tag{A20}$$

Consider the real part of the second term and define $\Delta_t = \sqrt[4]{\Delta_s^2 + 4\Delta_g^2}$:

$$\text{Re}\left(\frac{d\Delta_t}{d\Delta_s}\right) = -\frac{1}{\sqrt{2}(\Delta_s^2 + 4\Delta_g^2)^{1/4}}\sqrt{1 + \frac{\Delta_g}{\sqrt{\Delta_g^2 + \Delta_s^2}}}. \tag{A21}$$

We then have

$$\begin{aligned}\text{Re}\left(\frac{d\Delta}{d\Delta_s}\right) &= \sqrt{\frac{\Gamma}{\Delta_s}} \quad \text{when } \Delta_g = 0 \\ &= \frac{1}{2} \pm \sqrt{\frac{\Gamma}{\Delta_g}} \quad \text{when } \Delta_s \ll \Delta_g.\end{aligned} \tag{A22}$$

This means that the EP system has a frequency dependence of $\Delta \propto \sqrt{\Delta_s}$ and $\xi^{(1)} \propto 1/\sqrt{\Delta_g}$, which is different with the BP where $\Delta \propto \Delta_s^{1/3}$ and $\xi^{(1)} \propto 1/\Delta_g$.

4. Noise analysis

Now we include the thermal noise that drives the system in the semiclassical limit. Other noise sources can be included in the same way.

$$\begin{aligned}\dot{\alpha} - i\Delta\alpha &= -(\kappa/2 - [G - \gamma_s|\alpha|^2])\alpha - igs + \varphi(t), \\ \dot{s} - i\Delta s &= -[\Gamma/2 + i\Delta_s]s - ig\alpha + \eta(t).\end{aligned} \tag{A23}$$

The steady states solve these equations without the noise. So we are going to write our steady-state values as

$$\begin{aligned}\alpha &= \alpha_{\text{ss}} + \delta\alpha, \\ s &= s_{\text{ss}} + \delta s.\end{aligned} \tag{A24}$$

The noise spectrum we want to solve in the frequency domain could be expressed as

$$\begin{pmatrix} \delta\alpha \\ \delta s \end{pmatrix} = \begin{pmatrix} 2\delta - 3\frac{g^2}{R} - i\Delta & ig \\ ig & R - i\Delta \end{pmatrix}^{-1} \times \begin{pmatrix} \varphi_{\text{r}}(\Delta) + i\varphi_{\text{i}}(\Delta) \\ \eta_{\text{r}}(\Delta) + i\eta_{\text{i}}(\Delta) \end{pmatrix}. \tag{A25}$$

The spectra of the thermal noise sources are

$$\langle\varphi_{\text{r}}(\Delta)\varphi_{\text{r}}(\Delta')\rangle = \langle\varphi_{\text{i}}(\Delta)\varphi_{\text{i}}(\Delta')\rangle = \sqrt{\frac{\delta n_{\text{T}}}{2}}\delta(\Delta + \Delta'), \tag{A26}$$

$$\langle\eta_{\text{r}}(\Delta)\eta_{\text{r}}(\Delta')\rangle = \langle\eta_{\text{i}}(\Delta)\eta_{\text{i}}(\Delta')\rangle = \sqrt{\frac{Rn_{\text{T}}}{2}}\delta(\Delta + \Delta'). \tag{A27}$$

The imaginary part of $\delta\alpha$ could be defined as $\delta y \equiv -i(\delta\alpha - \delta\alpha^*)$, and could be expressed as

$$\delta y(\Delta) = \frac{\Delta(\Gamma/2+2\delta-3\frac{g^2}{\Gamma/2})[\Gamma/2\varphi_r(\Delta)+\Delta\varphi_i(\Delta)+g\eta_i(\Delta)]}{(\Gamma\delta-2g^2+\Delta^2)^2+\Delta^2(\Gamma/2+2\delta-3\frac{g^2}{\Gamma/2})^2} + \frac{(\Gamma\delta-2g^2+\Delta^2)(\Gamma/2\varphi_i(\Delta)-\Delta\varphi_r(\Delta)-g\eta_r(\Delta))}{(\Gamma\delta-2g^2+\Delta^2)^2+\Delta^2(\Gamma/2+2\delta-3\frac{g^2}{\Gamma/2})^2}, \tag{A28}$$

with $\delta \equiv G - \kappa/2$. This means that the BP system offers the advantage over EPs to not amplify the phase noise of the MFCs with the same amount of the small-signal amplification.

5. Multifield mixing

While we have focused on a frequency comb producing harmonics of a single tone drive, the analysis could be extended to three-field or multifield mixing scenario. Here we consider two modulation fields B_1 and B_2 are simultaneously applied at distinct frequencies ω_1 and ω_2 in the linear approximation. In this case, the time-dependent voltage is generalized as follows:

$$v(t) = V_0 \cos\left[\gamma_e B_0 t + \frac{\sqrt{2}\gamma_e B_1}{\omega_1}\sin(\omega_1 t) + \frac{\sqrt{2}\gamma_e B_2}{\omega_2}\sin(\omega_2 t)\right]. \tag{A29}$$

Applying the Jacobi-Anger expansion separately to each sinusoidal modulation, we derive a generalized double summation involving Bessel functions:

$$\cos[\omega_c t + \beta_1 \sin(\omega_1 t) + \beta_2 \sin(\omega_2 t)] = \sum_{k=-\infty}^{\infty}\sum_{l=-\infty}^{\infty} J_k(\beta_1)J_l(\beta_2)\cos[(\omega_c + k\omega_1 + l\omega_2)t], \tag{A30}$$

where the modulation indices β_1 and β_2 are defined as $\beta_1 = \sqrt{2}\gamma_e B_1/\omega_1$ and $\beta_2 = \sqrt{2}\gamma_e B_2/\omega_2$. This analysis could easily be extended to the nonlinear regime around BP as discussed in Appendixes A 1 and A 2.

6. Maxwell-Bloch equations for cavity-coupled NV ensemble

Here, we discuss how to tune the coupling strength g and spin linewidth Γ from the input field. We start from a theoretical description of the nonlinear model used to characterize the linear NV cavity quantum electrodynamics (cQED) system [55]. We begin with the interaction Hamiltonian between a microwave mode and an NV spin ensemble. We treat the system as an ensemble of two-level systems since the degeneracy of the $m_s = \pm 1$ NV ground-state spin levels is removed by applying an external magnetic bias field. Consequently, one spin transition is brought near resonance with the microwave mode and drive, while the other remains far off resonance. Incorporating the coherent drive, the Hamiltonian is expressed as [56,73]

$$H = \omega_c a^\dagger a + \sum \omega_j \sigma_j^\dagger \sigma_j + \sum g_s(a^\dagger \sigma_j + a\sigma_j^\dagger) + i\sqrt{\kappa_{c1}}\beta_{in}(a^\dagger e^{-i\omega_d t} - a e^{i\omega_d t}), \tag{A31}$$

where a is the lowering operator for the cavity field, σ_j is the lowering operator of jth NV spin, g_s is the single photon coupling strength, ω_c is the cavity frequency, ω_j is the frequency of jth NV spin, κ_{c1} is the cavity input loss, ω_d is the driving frequency. The input microwave drive field β_{in} is related to the power incident on the impedance-matching stub tuner P by $|\beta_{in}| = \sqrt{P/\hbar\omega_d}$.

The inhomogeneous NV ensemble is assumed to have a transverse relaxation rate $\gamma/2$ and an optically induced polarization rate γ_p. The cavity system is characterized by a total loss rate κ and an input-coupling loss rate κ_{c1}. Under the semiclassical approximation, assuming factorization of expectation values of products of system operators, the Bloch-Maxwell equations of motion for the cavity field, spin coherence, and polarization are given by [74]

$$\dot{\alpha} = -\left(i\Delta + \frac{\kappa}{2}\right)\alpha - ig_s\sum_j s_j + \sqrt{\kappa_{c1}}\beta_{in}, \tag{A32a}$$

$$\dot{s}_j = -\left(i\Delta_j + \frac{\gamma}{2}\right)s_j - ig_s\mathcal{P}_j\alpha, \tag{A32b}$$

$$\dot{\mathcal{P}}_j = -\gamma_p(\mathcal{P}_j - \bar{\mathcal{P}}) - 2ig_s(s_j\alpha^* - s_j^*\alpha). \tag{A32c}$$

Here α is the expectation value for the cavity field, $\mathcal{P}_j = p_{0j} - p_{1j}$ is the polarization—the population difference between the $m_s = 0$ (p_{0j}) and $m_s = 1$ (p_{1j}) populations, $\Delta = \omega_c - \omega_d$ is the cavity detuning, and $\Delta_j = \omega_j - \omega_d$ is the spin detuning for the jth spin. The polarization of the ensemble in the absence of the microwave drive is $\bar{\mathcal{P}}$. We are interested in the steady-state solution:

$$\alpha = \frac{\sqrt{\kappa_{c1}}\beta_{in} - ig_s\sum_j s_j}{\kappa/2 + i\Delta},$$
$$s_j = -i\mathcal{P}_j g_s \alpha \frac{1}{\gamma/2 + i\Delta_j},$$
$$\mathcal{P}_j = \bar{\mathcal{P}}_j - \frac{2ig_s}{\gamma_p}(\alpha^* s_j - \alpha s_j^*). \tag{A33}$$

Eliminating $\mathcal{P}_j$ from the cavity field equation yields

$$\alpha = \frac{\sqrt{\kappa_{c1}}\beta_{in}}{i\Delta + \frac{\kappa}{2} + g_s^2 \sum_j \frac{-i\Delta_j + \gamma/2}{\Delta_j^2 + \frac{\gamma^2}{4} + 2g_s^2|\alpha|^2\gamma/\gamma_p}}. \tag{A34}$$

Next we define $\chi = \sqrt{1 + [(8g_s^2|\alpha|^2)/(\gamma\gamma_p)]}$ to parametrize the degree of spin nonlinearity in the system. The argument, $8g_s^2|\alpha|^2/\gamma_p\gamma$, is analogous to the standard saturation parameter: For $8g_s^2|\alpha|^2 \ll \gamma\gamma_p$ (equivalently, $\chi \sim 1$), the system is described by linear response. For an ensemble of $N \gg 1$ NV centers with $m_s = 1$ transition frequency distributed according to $P(\omega')$, we could take a continuum limit to find

$$\alpha = \frac{\sqrt{\kappa_{c1}}\beta_{in}}{i\Delta + \frac{\kappa}{2} + g^2 \int \frac{\gamma/2 - i(\omega' - \omega_d)}{(\omega - \omega')^2 + \chi^2\gamma^2/4} P(\omega')d\omega'}, \tag{A35}$$

where we have introduced the collective coupling strength $g = \sqrt{N}g_s$ between the ensemble and the cavity. Equation (A35) represents the formal solution for the coupling between the dielectric resonator and the optically polarized spin ensemble with inhomogeneous broadening. As discussed in the main text, both sides of the equation contain α, indicating that the energy oscillates between the cavity photon and the NV ensemble.

For a Lorentzian-distributed ensemble,

$$P_L(\omega) = \frac{1}{2\pi\Gamma_0} \frac{\Gamma_0^2}{(\omega - \omega_s)^2 + \Gamma_0^2/4}. \tag{A36}$$

In the nonlinear regime, the integration yields a slightly more cumbersome expression:

$$\int \frac{\gamma/2 - i(\omega' - \omega_d)}{\gamma^2/4 + (\omega' - \omega_d)^2 + \gamma^2(\chi^2 - 1)/4} P_L(\omega')d\omega' = \frac{2\gamma + 2\Gamma_0/\chi - 4i\Delta_d}{(\Gamma_0 + \chi\gamma)^2 + 4\Delta_d^2}. \tag{A37}$$

At this point, we introduce an effective ensemble linewidth, $\Gamma = \Gamma_0 + \chi\gamma$, and collective coupling strength, $g_{eff} = g/\sqrt{\chi}$, to account for power broadening and quenching of the NV ensemble due to the microwave drive. This is the tuning mechanism of the coupling strength and the spin linewidth for the coupled NV-cavity system.

7. Two-field mixing in NV cQED system

To simplify the problem, we start from the cavity reflection coefficient with on resonance condition $\Delta = 0$. Numerical simulations are performed to demonstrate that the on resonant condition provides the best sensitivity. The reflection coefficient for such a system could be expressed as

$$r = -1 + \frac{\kappa_{c1}}{\kappa/2 + i\Delta + g^2 \frac{2\gamma + 2\Gamma/\chi - 4i\Delta_s}{(\Gamma + \chi\gamma)^2 + 4\Delta_s^2}} = -1 + \frac{\kappa_{c1}}{A} \frac{\Gamma_1^2 + 4\Delta_s^2}{1 + \frac{1}{A}(2\kappa\Delta_s^2 - 4ig\Delta_s)}, \tag{A38}$$

with $A \equiv (\kappa/2)\Gamma_1^2 + 2\Gamma_1 g_{eff}^2$. The Taylor expansion of Eq. (A38) shows

$$\begin{aligned} r &= -1 + \frac{\kappa_{c1}}{A} \frac{\Gamma_1^2 + 4\Delta_s^2}{1 + \frac{1}{A}(2\kappa\Delta_s^2 - 4ig\Delta_s)} \\ &= -1 + \frac{\kappa_{c1}}{A}(\Gamma_1^2 + 4\Delta_s^2)\left(1 - \frac{1}{A}(2\kappa\Delta_s^2 - 4ig^2\Delta_s) + \frac{1}{A^2}(2\kappa\Delta_s^2 - 4ig^2\Delta_s)^2 - \frac{1}{A^3}(2\kappa\Delta_s^2 - 4ig^2\Delta_s)^3\right) \\ &= -1 + \frac{\kappa_{c1}\Gamma_1^2}{A} + i\frac{4g^2\kappa_{c1}\Gamma_1^2}{A^2}\Delta_s - \frac{\kappa_{c1}\Gamma_1^2}{A}\left(\frac{2\kappa}{A} + \frac{16g^4}{A^2}\right)\Delta_s^2 - i\left(\frac{16\kappa_{c1}\Gamma_1^2}{A^3}\kappa g^2 + \frac{64g^6\kappa_{c1}\Gamma_1^2}{A^4} - \frac{16\kappa_{c1}g^2}{A^2}\right)\Delta_s^3, \end{aligned} \tag{A39}$$

Here we observe that the reflection coefficient is not linear with the detuning Δ_s. The imaginary (real) part of the reflection coefficient is proportional to Δ_s^{2n+1} (Δ_s^{2n}). If two fields with frequency ω_s and ω_d are injected into the system, the output field will have a frequency of $\omega_s \pm 2n\omega_d$ [$\omega_s \pm (2n+1)\omega_d$] for the channels I (Q), respectively, as shown in Fig. 7(a) [Fig. 7(b)]. In Fig. 7(c), we provide an exemplary frequency spectrum for the harmonics generated with frequency $\omega_s = 10^5$ Hz and $\omega_d = 100$ Hz. Both of the fields are set to be $B = 3.6$ μT. The number of teeth for such a system is 7. As a comparison, the BP-enhanced NV MFC system could generate a number of satellites of 300 given $B = 0.3$ μT.

Although the linear NV cQED system shows promising mixing, the system needs a large bias power (or equivalently LO power) to drive the system out of the linear range. The linear range of the NV cQED system is around the inhomogeneous linewidth Γ, which is around 330 kHz in the current system. The power consumption or the threshold for the nonlinearity is still large in such a linear NV cQED system.

8. Experimental setup

The experimental setup is illustrated in Fig. 8, comprising two main components: a microwave loop oscillator circuit and an optically pumped diamond-cavity interface. The diamond-cavity configuration closely follows our previous implementations [55,60], with the primary modification being the inclusion of an external signal generator that applies a drive field necessary for frequency comb generation. The diamond used (3 mm × 3 mm × 0.9 mm, 4 ppm NV ensemble, sourced from element 6) is positioned at the maximum of the TE01δ mode at the center of a

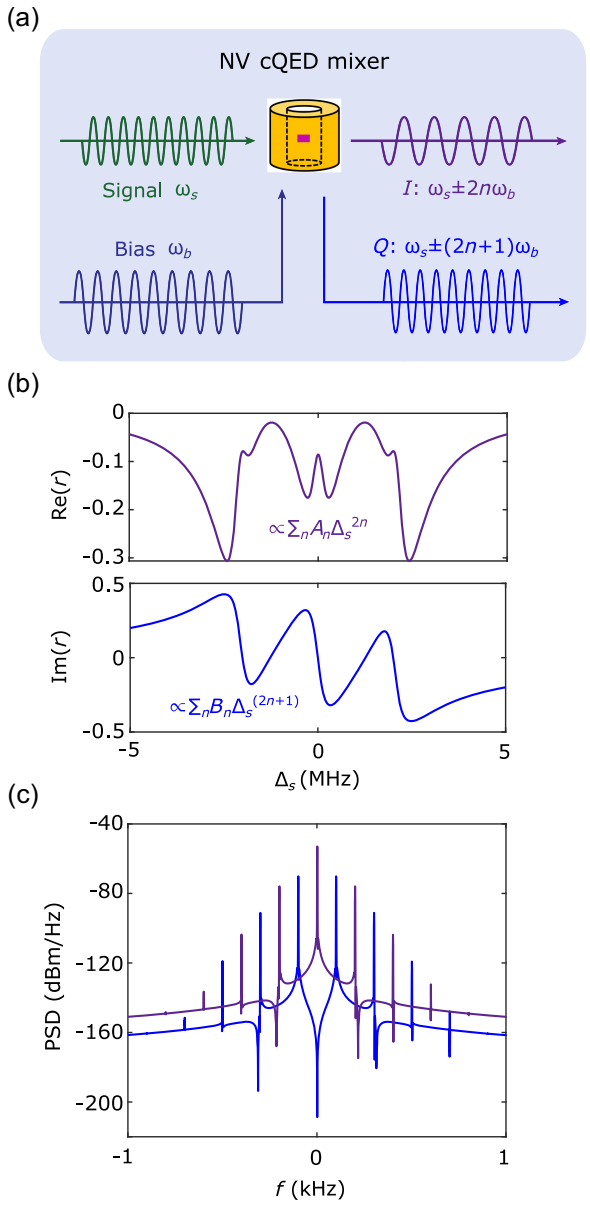


FIG. 7. NV cQED mixing and comb generation. (a) The NV cQED mixing scheme. A signal field with frequency ω_s and a bias field with frequency ω_d are applied to the NV cQED system. The in-phase and quadrature-phase outputs produce signals with frequencies $\omega_s \pm 2n\omega_d$ and $\omega_s \pm (2n+1)\omega_d$, respectively. (b) The reflection coefficient r as a function of cavity-spin detuning Δ_s. The real part (imaginary part) of the reflection coefficient could be expressed as $\sum_n A_n \Delta_s^{2n}$ ($\sum_n B_n \Delta_s^{2n+1}$). (c) An exemplary frequency comb generated with the NV cQED system.

high-permittivity dielectric resonator (Skyworks, $\varepsilon_r \sim 31$; material, D-87XX). A 4H-SiC wafer provides thermal management and mechanical support beneath the diamond, while two slabs of low-loss polytetrafluoroethylene (PTFE) secure and align the resonator in place. The entire assembly is enclosed in an aluminum housing to shield it from ambient electromagnetic interference (e.g., WiFi and 1.9 GHz 3G

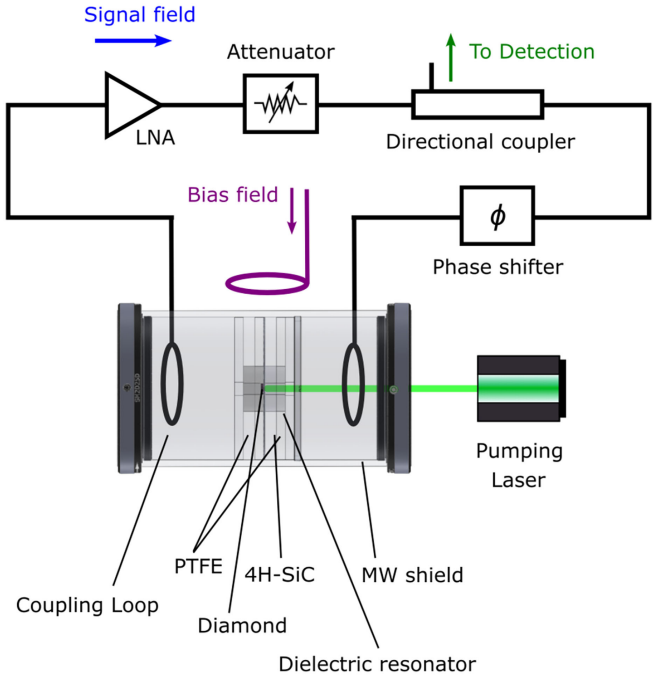


FIG. 8. Experimental setup for NV MFC. A 532-nm green laser is applied to the cavity-coupled diamond system. A bias field is generated by an external signal generator, while a self-oscillating signal field is initialized by the round-loop gain. A phase shifter is applied to fulfill the zero-phase requirement in the Barkhausen criteria, while a directional coupler is added to guide a part of the signal for detection. Note, LNA, low noise amplifier; MW, microwave.

signals) and minimize radiative losses. Optical spin polarization is achieved using a 532-nm, 8-W pump laser (Lighthouse Sprout-G). A three-axis coil system (not shown) applies the external static magnetic bias field.

The microwave circuitry consists of a cascade of amplification and attenuation stages. A 10:1 directional coupler (PE2CP1102) is placed within the chain to divert a portion of the signal outside the self-oscillating loop for analysis. This configuration of low-noise amplifiers and fixed attenuators ensures that the loop gain exceeds the total loss, enabling sustained oscillation, while the tunable attenuator allows fine control over the steady-state oscillation power. To characterize the output signal, both a spectrum analyzer and a custom heterodyne receiver are employed. The extracted signal from the directional coupler is mixed down to an intermediate frequency (IF) using a mixer driven by an external local oscillator. The resulting IF signal is then digitized by a data acquisition system and the power spectral density of the voltage is calculated via digital signal processing. We then determine the number of satellites by comparing the "signal" power with a bandwidth of 2 Hz at each satellite position ($\omega = n\omega_d$) to the average power with a 100-Hz bandwidth as a measure of the local noise floor. In this work, we use a measurement time of 0.5 s (bandwidth

2 Hz), which surpasses the oscillator linewidth (4.9 Hz), so that the SNR of each satellite will not increase with further measurement time. We note that the measured comb power depends sensitively on the frequency-axis offset, defined by the center frequency of the measurement window. When this offset is zero, symmetry enforces the disappearance of the even-order terms in the phase spectrum. In an unshielded environment, however, the offset is not fixed but distributed due to environmental fluctuations [as shown in Fig. 3(c), for example]. To minimize the impact of this effect, we report the largest observed comb power obtained during a continuous 10-s measurement in Figs. 3(d) and 3(e). We emphasize that this effect does not alter the core figure of merit, the number of comb teeth N_t defined in the main text, since this metric is determined by the spectral envelope rather than the detailed distribution of individual teeth.

9. Drive field delivery

We use a coil with a variable-amplitude function generator to apply the drive magnetic field. The coil has 50 turns with a resistance of 3 Ω, radius $R_0 = 2.2$ cm, and the distance to the diamond ensemble is measured to be $d = 2.3$ cm, while the function generator has a $R = 50$ Ω load. This results in a power-to-field relation of 67 $\mu T/\sqrt{W}$. Considering the angle between the applied magnetic field [100] and the NV axis [111], the power-to-field conversion ratio applied to NVs is 39 $\mu T/\sqrt{W}$. Here we use the total power output of the drive function generator with 50Ω resistance as a figure of merit, which offers significant room for improvement by increasing delivery efficiency as most power is dissipated in the terminating resistor.

In the experiment shown in Figs. 3 and 4, we applied a current with $I = 0.64$ mA for a magnetic field of 0.307 μT. The power consumption for such a system is calculated to be $P = I^2R = 21$ μW, or −16.6 dBm. The magnetic field is calibrated by the NV-based sensor presented in our previous work [55]. During the experiment process, we first calculate the power-to-field conversion ratio based on the measurement and the power sent to the system. Then we applied the currents needed for the specific magnetic fields shown in Figs. 3 and 4.

10. Power consumption discussions

Another practical figure of merit for evaluating different architectures is the total wall-plug power consumption. Although this metric does not affect the underlying physics explored in this work, it is relevant for future integrated or portable implementations. In our system, the primary dc power consumption arises from two components: (i) the low-noise amplifier used for frequency mixing and microwave field component generation and (ii) the optical excitation required to polarize the NV spin ensemble. Below we provide a brief comparison between our implementation and representative previous systems.

Here we compare our system with other MFCs generated by the coupled mode systems. We take Ref. [48] as an example. This work employs two signal generators to establish the required frequency mixing: Our setup uses a single microwave signal source combined with a compact low-noise amplifier. This approach provides a significantly lower wall-plug power overhead: A commercial microwave signal generator typically consumes on the order of 300 W (e.g., Keysight N5166B), whereas the compact amplifier used here dissipates approximately 1 W. For realistic applications, this reduction in electronic power overhead is advantageous for both thermal management and system integration.

NV-based systems require optical excitation for spin polarization. However, this requirement is not fundamentally more power intensive than the auxiliary resources needed in ferrimagnetic platforms. Ferrimagnetic systems generally require a large static magnetic field in the 0.1–0.3 T range for magnetization, which in practice is supplied by electromagnets or bias coils that also have nonnegligible dc power consumption. Similarly, both platforms require microwave or optical fields with their own electronic overhead for generating pump and probe tones. Optical frequency comb systems, for example, rely on lasers whose wall-plug power far exceeds their output optical power.

Overall, for most practical implementations across platforms—including those based on NV centers, ferrimagnets, and optical combs—the dc power consumed by auxiliary electronics (lasers, amplifiers, signal generators, and magnetic-field sources) dominates over the microwave power delivered to the mixing element itself. Thus, while wall-plug power is an important engineering consideration for future system miniaturization, its contribution is largely determined by ancillary components rather than the intrinsic nonlinear physics explored in this work.

[1] S. A. Diddams, K. Vahala, and T. Udem, *Optical frequency combs: Coherently uniting the electromagnetic spectrum*, Science **369**, eaay3676 (2020).
[2] D. I. Herman, M. Walsh, M. K. Kreider, N. Lordi, E. J. Tsao, A. J. Lind, M. Heyrich, J. Combes, J. Genest, and S. A. Diddams, *Squeezed dual-comb spectroscopy*, Science **387**, 653 (2025).
[3] V. Brasch, M. Geiselmann, T. Herr, G. Lihachev, M. H. Pfeiffer, M. L. Gorodetsky, and T. J. Kippenberg, *Photonic chip-based optical frequency comb using soliton Cherenkov radiation*, Science **351**, 357 (2016).
[4] L. Chang, S. Liu, and J. E. Bowers, *Integrated optical frequency comb technologies*, Nat. Photonics **16**, 95 (2022).
[5] S. Sun, B. Wang, K. Liu, M. W. Harrington, F. Tabatabaei, R. Liu, J. Wang, S. Hanifi, J. S. Morgan, M. Jahanbozorgi

et al., *Integrated optical frequency division for microwave and mmWave generation*, Nature (London) **627**, 540 (2024).
[6] A. L. Gaeta, M. Lipson, and T. J. Kippenberg, *Photonic-chip-based frequency combs*, Nat. Photonics **13**, 158 (2019).
[7] J. S. Ochs, D. K. J. Boneß, G. Rastelli, M. Seitner, W. Belzig, M. I. Dykman, and E. M. Weig, *Frequency comb from a single driven nonlinear nanomechanical mode*, Phys. Rev. X **12**, 041019 (2022).
[8] T.-Y. Chen, C.-P. Tsai, and W.-C. Li, *Ultrasensitive sensing via internal resonance induced frequency combs in micromechanical resonators*, J. Microelectromech. Syst. **34**, 557 (2025).
[9] L. Colombo, H. M. Hussein, W. Gubinelli, R. Tetro, N. Casilli, A. Banfi, P. Simeoni, M. Rinaldi, and C. Cassella, *A passive wireless quasi-harmonic strain sensor for eternal structural health monitoring*, in *2024 IEEE Sensors, Kobe, Japan* (IEEE, New York, 2024), pp. 1–4.
[10] P. Srivastava, P. P. Kumar, and C. V. Rao, *Design and development of multi-frequency comb generator for space borne microwave active sensors*, in *Proceedings of the 2008 International Conference on Recent Advances in Microwave Theory and Applications, Jaipur, India* (IEEE, New York, 2008), pp. 445–447.
[11] H. Wu, Z. Qian, H. Zhang, X. Xu, B. Xue, and J. Zhai, *Precise underwater distance measurement by dual acoustic frequency combs*, Ann. Phys. (Berlin) **531**, 1900283 (2019).
[12] A. Greco, X. Ballu, F. Giazotto, and A. Crippa, *Coherent microwave comb generation via the Josephson effect*, arXiv:2503.13259.
[13] J. Guo, J. Xu, and C. Qian, *Design of dual-mode frequency multiplier with Schottky diodes*, IEEE Microwave Wireless Compon. Lett. **24**, 554 (2014).
[14] L. Xiang, Y. Zhu, Q. Ding, Y. Luo, J. Sun, Z. Zeng, J. Zhang, X. Li, L. Jin, Y. Shangguan *et al.*, *A microwave comb generator based on AGaN/GaN heterostructure Schottky diodes nonlinear transmission line*, Appl. Phys. Express **16**, 074001 (2023).
[15] M. Saeed, A. Hamed, P. Palacios, B. Uzlu, Z. Wang, E. Baskent, and R. Negra, *Voltage-tunable thin film graphene-diode-based microwave harmonic generator*, IEEE Microwave Wireless Compon. Lett. **31**, 733 (2021).
[16] R. K. Rai and N. Lohchaab, *Higher order harmonic generation using capacitive nonlinearity of the step recovery diode*, in *Proceedings of the 2023 IEEE Microwaves, Antennas, and Propagation Conference (MAPCON), Ahmedabad, India* (IEEE, New York, 2023), pp. 1–4.
[17] Q. Li, W. Jiang, Y. Xu, and F. Nian, *Analysis and design of wide-band comb generator based on srd*, in *Proceedings of the 2012 International Conference on Microwave and Millimeter Wave Technology (ICMMT), Shenzhen, China* (IEEE, New York, 2012), Vol. 1, pp. 1–3.
[18] T. Micallef, X. Gu, and K. Wu, *Diode-based wideband harmonic generation for future nonlinear sensing applications*, IEEE Trans. Microwave Theory Tech. **73**, 6180 (2025).
[19] Z. Wang, H. Y. Yuan, Y. Cao, Z.-X. Li, R. A. Duine, and P. Yan, *Magnonic frequency comb through nonlinear magnon-skyrmion scattering*, Phys. Rev. Lett. **127**, 037202 (2021).
[20] C. Zhao, Z. Yang, R. Peng, J. Yang, C. Li, and L. Zhou, *Dissipative-coupling-induced transparency and high-order sidebands with Kerr nonlinearity in a cavity-magnonics system*, Phys. Rev. Appl. **18**, 044074 (2022).
[21] T. Hula, K. Schultheiss, F. J. T. Goncalves, L. Körber, M. Bejarano, M. Copus, L. Flacke, L. Liensberger, A. Buzdakov, A. Kákay *et al.*, *Spin-wave frequency combs*, Appl. Phys. Lett. **121** (2022).
[22] J. W. Rao, B. Yao, C. Y. Wang, C. Zhang, T. Yu, and W. Lu, *Unveiling a pump-induced magnon mode via its strong interaction with Walker modes*, Phys. Rev. Lett. **130**, 046705 (2023).
[23] G.-T. Xu, M. Zhang, Y. Wang, Z. Shen, G.-C. Guo, and C.-H. Dong, *Magnonic frequency comb in the magnomechanical resonator*, Phys. Rev. Lett. **131**, 243601 (2023).
[24] Y.-S. Juan and F.-Y. Lin, *Microwave-frequency-comb generation utilizing a semiconductor laser subject to optical pulse injection from an optoelectronic feedback laser*, Opt. Lett. **34**, 1636 (2009).
[25] A. Ganesan and A. Seshia, *Resonance tracking in a micromechanical device using phononic frequency combs*, Sci. Rep. **9**, 9452 (2019).
[26] W. S. Wall, R. L. Kubena, Y.-K. Yook, J. Koehl, and R. J. Joyce, *Phase noise transfer in high-Q quartz phononic frequency combs*, in *Proceedings of the 2020 IEEE International Ultrasonics Symposium (IUS), Las Vegas, NV, USA* (IEEE, New York, 2020), pp. 1–4.
[27] M. H. De Jong, A. Ganesan, A. Cupertino, S. Gröblacher, and R. A. Norte, *Mechanical overtone frequency combs*, Nat. Commun. **14**, 1458 (2023).
[28] A. Ganesan, C. Do, and A. Seshia, *Frequency transitions in phononic four-wave mixing*, Appl. Phys. Lett. **111** (2017).
[29] P. Song, J. Wu, S. Zang, E. Abdel-Rahman, L. Shao, and W. Zhang, *Strong nonlinear mixing evolutions within phononic frequency combs*, Commun. Nonlinear Sci. Numer. Simul. **138**, 108233 (2024).
[30] H. Hodaei, A. U. Hassan, S. Wittek, H. Garcia-Gracia, R. El-Ganainy, D. N. Christodoulides, and M. Khajavikhan, *Enhanced sensitivity at higher-order exceptional points*, Nature (London) **548**, 187 (2017).
[31] W. Chen, Ş. Kaya Özdemir, G. Zhao, J. Wiersig, and L. Yang, *Exceptional points enhance sensing in an optical microcavity*, Nature (London) **548**, 192 (2017).
[32] X. Yin and X. Zhang, *Unidirectional light propagation at exceptional points*, Nat. Mater. **12**, 175 (2013).
[33] Q. Song, M. Odeh, J. Zúñiga-Pérez, B. Kanté, and P. Genevet, *Plasmonic topological metasurface by encircling an exceptional point*, Science **373**, 1133 (2021).
[34] J. Doppler, A. A. Mailybaev, J. Böhm, U. Kuhl, A. Girschik, F. Libisch, T. J. Milburn, P. Rabl, N. Moiseyev, and S. Rotter, *Dynamically encircling an exceptional point for asymmetric mode switching*, Nature (London) **537**, 76 (2016).
[35] W. Liu, Y. Wu, C.-K. Duan, X. Rong, and J. Du, *Dynamically encircling an exceptional point in a real quantum system*, Phys. Rev. Lett. **126**, 170506 (2021).
[36] A. Li, H. Wei, M. Cotrufo, W. Chen, S. Mann, X. Ni, B. Xu, J. Chen, J. Wang, S. Fan *et al.*, *Exceptional points and non-Hermitian photonics at the nanoscale*, Nat. Nanotechnol. **18**, 706 (2023).

[37] B. Peng, Ş. Özdemir, S. Rotter, H. Yilmaz, M. Liertzer, F. Monifi, C. Bender, F. Nori, and L. Yang, *Loss-induced suppression and revival of lasing*, Science **346**, 328 (2014).
[38] B. Peng, Ş. K. Özdemir, M. Liertzer, W. Chen, J. Kramer, H. Yılmaz, J. Wiersig, S. Rotter, and L. Yang, *Chiral modes and directional lasing at exceptional points*, Proc. Natl. Acad. Sci. U.S.A. **113**, 6845 (2016).
[39] H. Nasari, G. Lopez-Galmiche, H. E. Lopez-Aviles, A. Schumer, A. U. Hassan, Q. Zhong, S. Rotter, P. LiKamWa, D. N. Christodoulides, and M. Khajavikhan, *Observation of chiral state transfer without encircling an exceptional point*, Nature (London) **605**, 256 (2022).
[40] F. Ding, Y. Deng, C. Meng, P. C. Thrane, and S. I. Bozhevolnyi, *Electrically tunable topological phase transition in non-Hermitian optical mems metasurfaces*, Sci. Adv. **10**, eadl4661 (2024).
[41] Y.-P. Ruan, J.-S. Tang, Z. Li, H. Wu, W. Zhou, L. Xiao, J. Chen, S.-J. Ge, W. Hu, H. Zhang *et al.*, *Observation of loss-enhanced magneto-optical effect*, Nat. Photonics **19**, 109 (2025).
[42] J. Xu, Y. Mao, Z. Li, Y. Zuo, J. Zhang, B. Yang, W. Xu, N. Liu, Z. J. Deng, W. Chen *et al.*, *Single-cavity loss-enabled nanometrology*, Nat. Nanotechnol. **19**, 1472 (2024).
[43] Y.-H. Lai, Y.-K. Lu, M.-G. Suh, Z. Yuan, and K. Vahala, *Observation of the exceptional-point-enhanced Sagnac effect*, Nature (London) **576**, 65 (2019).
[44] H.-K. Lau and A. A. Clerk, *Fundamental limits and non-reciprocal approaches in non-Hermitian quantum sensing*, Nat. Commun. **9**, 4320 (2018).
[45] W. Langbein, *No exceptional precision of exceptional-point sensors*, Phys. Rev. A **98**, 023805 (2018).
[46] R. Kononchuk, J. Cai, F. Ellis, R. Thevamaran, and T. Kottos, *Exceptional-point-based accelerometers with enhanced signal-to-noise ratio*, Nature (London) **607**, 697 (2022).
[47] H. Loughlin and V. Sudhir, *Exceptional-point sensors offer no fundamental signal-to-noise ratio enhancement*, Phys. Rev. Lett. **132**, 243601 (2024).
[48] C. Wang, J. Rao, Z. Chen, K. Zhao, L. Sun, B. Yao, T. Yu, Y.-P. Wang, and W. Lu, *Enhancement of magnonic frequency combs by exceptional points*, Nat. Phys. **20**, 1139 (2024).
[49] H. Wang, Y.-H. Lai, Z. Yuan, M.-G. Suh, and K. Vahala, *Petermann-factor sensitivity limit near an exceptional point in a Brillouin ring laser gyroscope*, Nat. Commun. **11**, 1610 (2020).
[50] J. Naikoo, R. W. Chhajlany, and J. Kołodyński, *Multiparameter estimation perspective on non-Hermitian singularity-enhanced sensing*, Phys. Rev. Lett. **131**, 220801 (2023).
[51] C. Chen, L. Jin, and R.-B. Liu, *Sensitivity of parameter estimation near the exceptional point of a non-Hermitian system*, New J. Phys. **21**, 083002 (2019).
[52] C. L. Degen, F. Reinhard, and P. Cappellaro, *Quantum sensing*, Rev. Mod. Phys. **89**, 035002 (2017).
[53] J. F. Barry, J. M. Schloss, E. Bauch, M. J. Turner, C. A. Hart, L. M. Pham, and R. L. Walsworth, *Sensitivity optimization for NV-diamond magnetometry*, Rev. Mod. Phys. **92**, 015004 (2020).
[54] H. Wang, M. E. Trusheim, L. Kim, H. Raniwala, and D. R. Englund, *Field programmable spin arrays for scalable quantum repeaters*, Nat. Commun. **14**, 704 (2023).
[55] H. Wang, K. L. Tiwari, K. Jacobs, M. Judy, X. Zhang, D. R. Englund, and M. E. Trusheim, *A spin-refrigerated cavity quantum electrodynamic sensor*, Nat. Commun. **15**, 10320 (2024).
[56] H. Wang, S. Wu, K. Jacobs, Y. Duan, D. R. Englund, and M. E. Trusheim, *Cavity-enhanced solid-state nuclear spin gyroscope*, Phys. Rev. Lett. **134**, 183603 (2025).
[57] E. R. Eisenach, J. F. Barry, M. F. O'Keeffe, J. M. Schloss, M. H. Steinecker, D. R. Englund, and D. A. Braje, *Cavity-enhanced microwave readout of a solid-state spin sensor*, Nat. Commun. **12**, 1357 (2021).
[58] Y. Zhang, Q. Wu, S.-L. Su, Q. Lou, C. Shan, and K. Mølmer, *Cavity quantum electrodynamics effects with nitrogen vacancy center spins coupled to room temperature microwave resonators*, Phys. Rev. Lett. **128**, 253601 (2022).
[59] H. Wu, S. Mirkhanov, W. Ng, and M. Oxborrow, *Bench-top cooling of a microwave mode using an optically pumped spin refrigerator*, Phys. Rev. Lett. **127**, 053604 (2021).
[60] H. Wang, K. Jacobs, D. Fahey, Y. Hu, D. R. Englund, and M. E. Trusheim, *Exceptional sensitivity near the bistable transition point of a hybrid quantum system*, Nat. Phys. (2026), 10.1038/s41567-026-03217-3.
[61] A. Suntharalingam, L. Fernández-Alcázar, R. Kononchuk, and T. Kottos, *Noise resilient exceptional-point voltmeters enabled by oscillation quenching phenomena*, Nat. Commun. **14**, 5515 (2023).
[62] K. Bai, L. Fang, T.-R. Liu, J.-Z. Li, D. Wan, and M. Xiao, *Nonlinearity-enabled higher-order exceptional singularities with ultra-enhanced signal-to-noise ratio*, Natl. Sci. Rev. **10**, nwac259 (2023).
[63] K. Bai, J.-Z. Li, T.-R. Liu, L. Fang, D. Wan, and M. Xiao, *Nonlinear exceptional points with a complete basis in dynamics*, Phys. Rev. Lett. **130**, 266901 (2023).
[64] K. Bai, T.-R. Liu, L. Fang, J.-Z. Li, C. Lin, D. Wan, and M. Xiao, *Observation of nonlinear exceptional points with a complete basis in dynamics*, Phys. Rev. Lett. **132**, 073802 (2024).
[65] S. Murali and P. Gupta, *Overmodulation protection in fm transmitters*, in *Proceedings of the 2013 National Conference on Communications (NCC), New Delhi, India* (IEEE, New York, 2013), pp. 1–5.
[66] J. F. Barry, R. A. Irion, M. H. Steinecker, D. K. Freeman, J. J. Kedziora, R. G. Wilcox, and D. A. Braje, *Ferrimagnetic oscillator magnetometer*, Phys. Rev. Appl. **19**, 044044 (2023).
[67] J. Luo, Y. Geng, F. Rana, and G. D. Fuchs, *Room temperature optically detected magnetic resonance of single spins in gan*, Nat. Mater. **23**, 512 (2024).
[68] T. Day, M. Isarov, W. J. Pappas, B. C. Johnson, H. Abe, T. Ohshima, D. R. McCamey, A. Laucht, and J. J. Pla, *Room-temperature solid-state maser amplifier*, Phys. Rev. X **14**, 041066 (2024).
[69] A. Angerer, S. Putz, D. O. Krimer, T. Astner, M. Zens, R. Glattauer, K. Streltsov, W. J. Munro, K. Nemoto, S. Rotter, J. Schmiedmayer, and J. Majer, *Ultralong relaxation times*

in bistable hybrid quantum systems, Sci. Adv. **3**, e1701626 (2017).

[70] D. O. Krimer, M. Zens, and S. Rotter, *Critical phenomena and nonlinear dynamics in a spin ensemble strongly coupled to a cavity. I. Semiclassical approach*, Phys. Rev. A **100**, 013855 (2019).

[71] M. Zens, D. O. Krimer, and S. Rotter, *Critical phenomena and nonlinear dynamics in a spin ensemble strongly coupled to a cavity. II. Semiclassical-to-quantum boundary*, Phys. Rev. A **100**, 013856 (2019).

[72] H. Wang, K. Jacobs, D. R. Englund, and M. E. Trusheim, *Data associated with "Ultralow-power microwave frequency comb at a bistable phase transition"*, https://github.com/hanfengw/NVMFC (2026).

[73] M. Blaha, A. Johnson, A. Rauschenbeutel, and J. Volz, *Beyond the Tavis-Cummings model: Revisiting cavity QED with ensembles of quantum emitters*, Phys. Rev. A **105**, 013719 (2022).

[74] M. O. Scully and M. S. Zubairy, *Quantum Optics* (Cambridge University Press, Cambridge, England, 1997).